C. R. Chimie 20 (2017) 467–474

Contents lists available at ScienceDirect

Comptes Rendus Chimie

www.sciencedirect.com

Full paper/Mémoire

Structural studies of bis(histidinato)nickel(II): Combined experimental and computational studies

Alireza Abbasi*, Barzin Safarkoopayeh, Nikoo Khosravi, Alireza Shayesteh

School of Chemistry, College of Science, University of Tehran, Tehran, Iran

ARTICLE INFO

Article history:
Received 6 August 2016
Accepted 20 December 2016
Available online 6 February 2017

Keywords:
Nickel(II) complex
Histidine
X-ray structure
DFT calculations
TD-DFT calculations
QTAIM analysis

ABSTRACT

A distorted octahedral nickel(II) complex, [Ni(2-amino-3-(1*H*-imidazol-4-yl)propanoic acid)$_2$] (**1**), has been synthesized by a solvothermal method and characterized by single-crystal X-ray diffraction. Geometry optimization in the gas phase and pyridine together with Hirshfeld surface and reduced density gradient analyses reveal that this complex shows different distortions from octahedral in the gas, liquid, and solid phases. The reason seems to be because of the presence of two intramolecular N–H···O weak interactions in the gas phase and two sets of rather strong intermolecular N–H···O and C–H···O interactions in the solid phase. Time-dependent density functional theory (TD-DFT) calculations suggest that these different distortions result in different electronic absorption spectra.

© 2016 Académie des sciences. Published by Elsevier Masson SAS. All rights reserved.

1. Introduction

In recent years, there has been an increasing interest in the syntheses of functional metal complexes having catalytic [1,2] and magnetic [3,4] properties or biological activities [5,6]. These complexes can be formed by using various multidentate ligands. Although less attention has been paid to Ni(II) complexes, they have various applications such as antibacterial activity, C–C and C–S cross-coupling, double-bond functionalization, and CO_2 reduction reaction [7,8]. Herein, we report synthesis of a novel Ni(II) complex, using histidine (2-amino-3-(1*H*-imidazol-4-yl) propanoic acid) as the chelating agent. Histidine is an α-amino acid with an imidazole functional group, first isolated by German physician Albrecht Kossel [9]. The conjugate acid (protonated form) of the imidazole side chain in histidine has a pK_a of approximately 6.0. For pH less than 6, the imidazole ring is mostly protonated [10], and the imidazole ring bears two NH bonds and has a positive charge. The positive charge is equally distributed between the two nitrogen atoms and can be represented with two equally important resonant structures. The imidazole ring of histidine is aromatic at all pH values [11]. It can have π stacking interactions [12], complicated by the positive charge [13]. The title compound was synthesized using the solvothermal method [14]. Solvothermal processes, using low or medium temperatures, can be considered as alternatives to the high temperature methods based in particular on melt growth or vapor growth processes. Furthermore, theoretical calculation can be used for structural elucidation [15–17]. In the present work, we report the newly synthesized bis(histidinato) nickel(II) complex, followed by TD-DFT, quantum theory of atoms in molecules (QTAIM), and reduced density gradient calculations.

2. Experimental section

2.1. Materials

All chemicals were purchased from commercial sources and used as received.

Compound **1** was prepared from the mixture of $NiCO_3 \cdot xH_2O$ (0.375 mmol), histidine (0.75 mmol), 4,4′-

* Corresponding author.
E-mail address: aabbasi@khayam.ut.ac.ir (A. Abbasi).

http://dx.doi.org/10.1016/j.crci.2016.12.006
1631-0748/© 2016 Académie des sciences. Published by Elsevier Masson SAS. All rights reserved.

bipyridine (0.375 mmol), and methanol/H_2O (2 mL with a ratio of 10:1). The suspension was stirred for 15 min and then transferred to a 23 mL Teflon-lined stainless steel autoclave followed by heating at 150 °C for 48 h. After slow cooling to room temperature, the product was filtered, washed with methanol, and dried in air. Elemental analysis calcd (%) for $NiC_{12}H_{16}N_6O_4 + 1\ H_2O$: C, 37.44%; H, 4.71%; N, 21.83%; O, 20.87%; found: C, 37.40%; H, 4.75%; N, 21.78%; O, 20.90%.

2.2. Crystal structure determination and refinement

The data were collected on Marresearch 345 dtb diffractometer using Mo Kα radiation (λ = 0.71073 Å) at 295 K. The structure was solved by direct methods using SHELXS-97 and the obtained model refined with SHELXL-97 [18]. All non-hydrogen atoms were refined anisotropically. Hydrogen atoms were added at ideal positions and refined using a riding model. The data were deposited in Cambridge Crystallographic Data Centre, with deposition number CCDC-979056. The Oak Ridge thermal ellipsoid plot (ORTEP) view of **1** and its selected crystallographic and experimental details are summarized in Fig. 1 and Table 1, respectively.

2.3. Thermal gravimetric analysis

The thermal properties of **1** were studied by Thermogravimetric analysis/Differential thermal analysis (TGA/DTA) in the temperature range 30–600 °C (Fig. 2). It showed that the complex is stable until 355 °C and starts to decompose at about 371 °C. The thermogram exhibits two distinct weight losses at 141 and 390 °C. The first weight loss at 141 °C could be ascribed to the loss of surface water. The second weight loss at 390 °C indicates loss of histidine ligands and decomposition of the complex.

3. Computational details

To get insight into the electronic structure of **1**, density functional calculations were carried out with the ORCA 3.0.3 program [19]. We used the PBE0 functional and the def2-TZVP (triple zeta valence polarized) basis sets to optimize the geometries in the gas phase and pyridine using the **CO**nductor-like **S**creening **MO**del (COSMO) solvation model [19]. Vibrational frequency calculations were carried on the optimized structures in solvent and gas phase, to confirm that both structures were minima. The electronic structure of the title compound was investigated by QTAIM and by reduced density gradient analysis using Multiwfn 3.7 program [20].

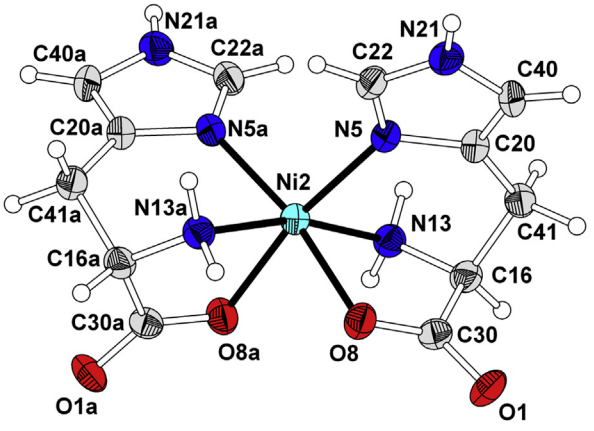

Fig. 1. ORTEP diagram of **1**. Thermal ellipsoids are drawn at the 50% probability level.

Table 1
Crystal and structure refinement data for bis(histidinato)nickel(II) (**1**).

Compound	**1**
Empirical formula	$C_{12}H_{16}N_6NiO_4$
Molecular weight	367.00
Crystal system	Tetragonal
Space group	$P4_32_12$
Temperature (K)	293(2)
$a = b$ (Å)	7.3157(10)
c (Å)	28.870(6)
$\alpha = \beta = \gamma$ (°)	90.00
Cell volume (Å^3)	1545.1(4)
Z	4
ρ (g cm^{-3})	1.578
μ (mm^{-1})	1.285
Total reflections	5255
Unique reflections	1465
Observed reflections [$F^2 > 2\sigma(F^2)$]	1292
Data/restraints/parameters	1465/0/121
Goodness-of-fit on F^2	1.068
R [$F^2 > 2\sigma(F^2)$] (R_1, wR_2)	0.0719, 0.1611
R (all data) (R_1, wR_2)	0.0830, 0.1735

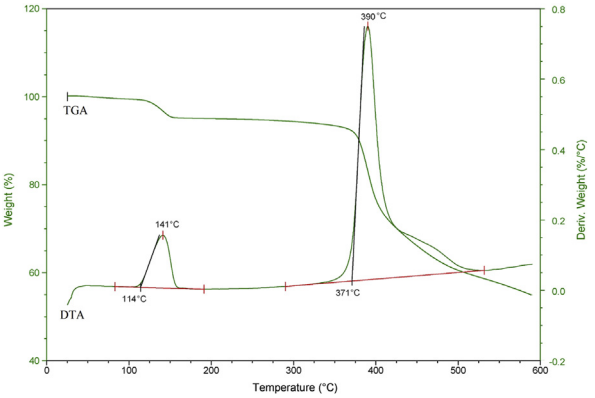

Fig. 2. TGA/DTA characterization.

4. Results and discussion

4.1. Molecular structure

Geometry optimization was started from the single crystal X-ray experimental atomic positions and the optimized geometric parameters (bond distances and bond angles) are given in Table 2. All of the bond lengths are slightly overestimated compared with the experimental values. By comparing the bond lengths, maximum deviations of 0.052 and 0.010 Å for Ni_2–O_8 were found for the optimized structure in the gas phase and pyridine,

Table 2
Selected bond lengths and angles around central nickel atom in **1**.

	Experimental	Optimized (gas)	Optimized (pyridine)
Bond[a] (Å)			
Ni_2–O_8	2.060	2.026	2.070
Ni_2–N_5	2.099	2.151	2.109
Ni_2–N_{13}	2.095	2.115	2.104
Angle (degree)			
O_{8a}–Ni_2–O_8	83.97	95.32	90.05
N_{13}–Ni_2–O_8	80.76	79.89	79.34
N_5–Ni_2–O_8	87.28	86.17	87.63
N_{13}–Ni_2–N_5	86.32	87.09	87.68
N_{13a}–Ni_2–N_5	103.17	107.79	104.29
N_{13a}–Ni_2–N_{13}	165.24	155.65	162.41

[a] Because of $P4_32_12$ space group contrary bonds are equivalent.

respectively. All bond lengths are in good agreement with their corresponding values from X-ray structural analysis, but the angles around central Ni(II) show rather high deviations. Maximum deviations of 11.35° and 6.08° for the O_{8a}–Ni_2–O_8 angle, 6.61° and 1.12° for N_{13a}–Ni_2–N_5, and 9.59° and 2.83° for N_{13a}–Ni_2–N_{13} were obtained for the optimized structure in the gas phase and pyridine, respectively. Further investigations revealed that this deviation originated from two sets of weak and moderate O···H intramolecular and intermolecular interactions present in the gas and solid phases, respectively. The presence of two intramolecular N–H···O weak interactions in the gas phase is responsible for increasing the N_{13a}–Ni_2–N_5 angle and decreasing the N_{13a}–Ni_2–N_{13} angle (Fig. 3). These

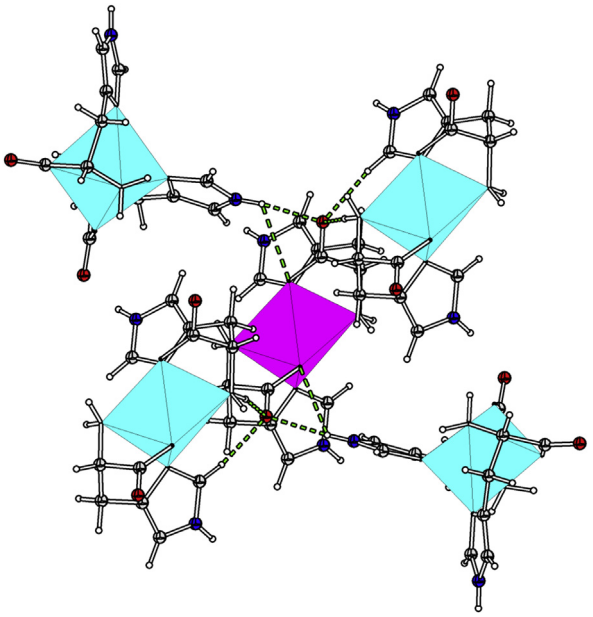

Fig. 4. The presence of two sets of bifurcated intermolecular N–H···O and C–H···O bonds between imidazole ring from four of the neighboring molecules and carboxyl groups of **1**.

interactions do not exist in the solid phase because of the participation of respected oxygen atoms in a stronger intermolecular hydrogen bond with neighboring molecules. By optimization of the structure in pyridine solvent,

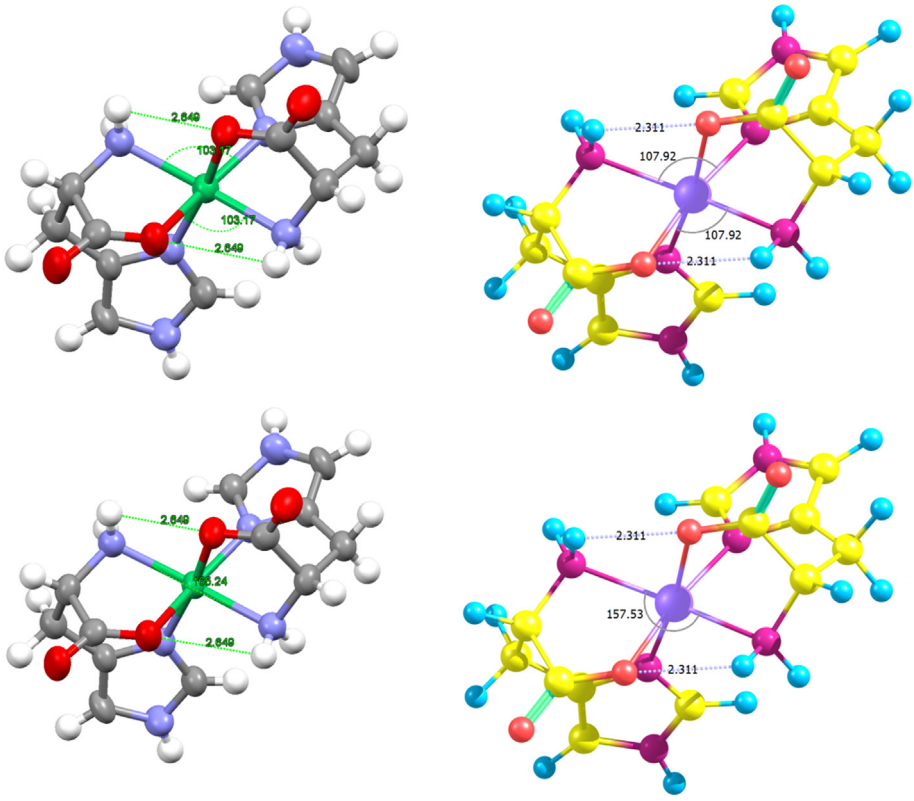

Fig. 3. The presence of two intramolecular weak interactions in the gas phase, which do not exist in solid phase.

Table 3
Hydrogen bonds specifications in the molecular crystal.

	H···A (Å)	D···A (Å)	D–H···A (degree)
N_{21b}–H···O_1	1.994	2.845	169.50
N_{21b}–H···O_8	2.596	3.062	115.09
N_{13b}–H···O_1	2.284	3.171	167.41
C_{22c}–H···O_1	2.125	3.043	169.14

the N_{13a}–Ni_2–N_5 and N_{13a}–Ni_2–N_{13} angles get closer to the experimental values. However, the O_{8a}–Ni_2–O_8 angle still shows rather high deviations and we discuss the reasons for this discrepancy in the following sections.

4.2. Hirshfeld surfaces

To gain further insight into the intermolecular interactions of molecular crystals, Hirshfeld surface [21–23] and the related two-dimensional (2D)-fingerprint plot [24–26] were calculated using the Crystal Explorer program [27]. Hirshfeld surface analysis reveals that the dominant interactions in the solid phase are two sets of bifurcated intermolecular N–H···O and C–H···O bonds between imidazole ring from four of the neighboring molecules and carboxyl groups of **1** (Fig. 4). The related data of these hydrogen bonds are summarized in Table 3. The presence of these hydrogen bonds has two effects on the solid phase geometry: the intramolecular N–H···O weak interactions disappear and the O_{8a}–Ni_2–O_8 angle becomes 83.97°.

The Hirshfeld surfaces were mapped with d_{norm} for **1** and the corresponding fingerprint plots are shown in Fig. 5. The dominant interaction in the molecular crystal is O···H and can be seen in the Hirshfeld surface as bright red areas. Two-dimensional fingerprint plots complement these surfaces, quantitatively summarizing the nature and type of intermolecular contacts experienced by molecules in the

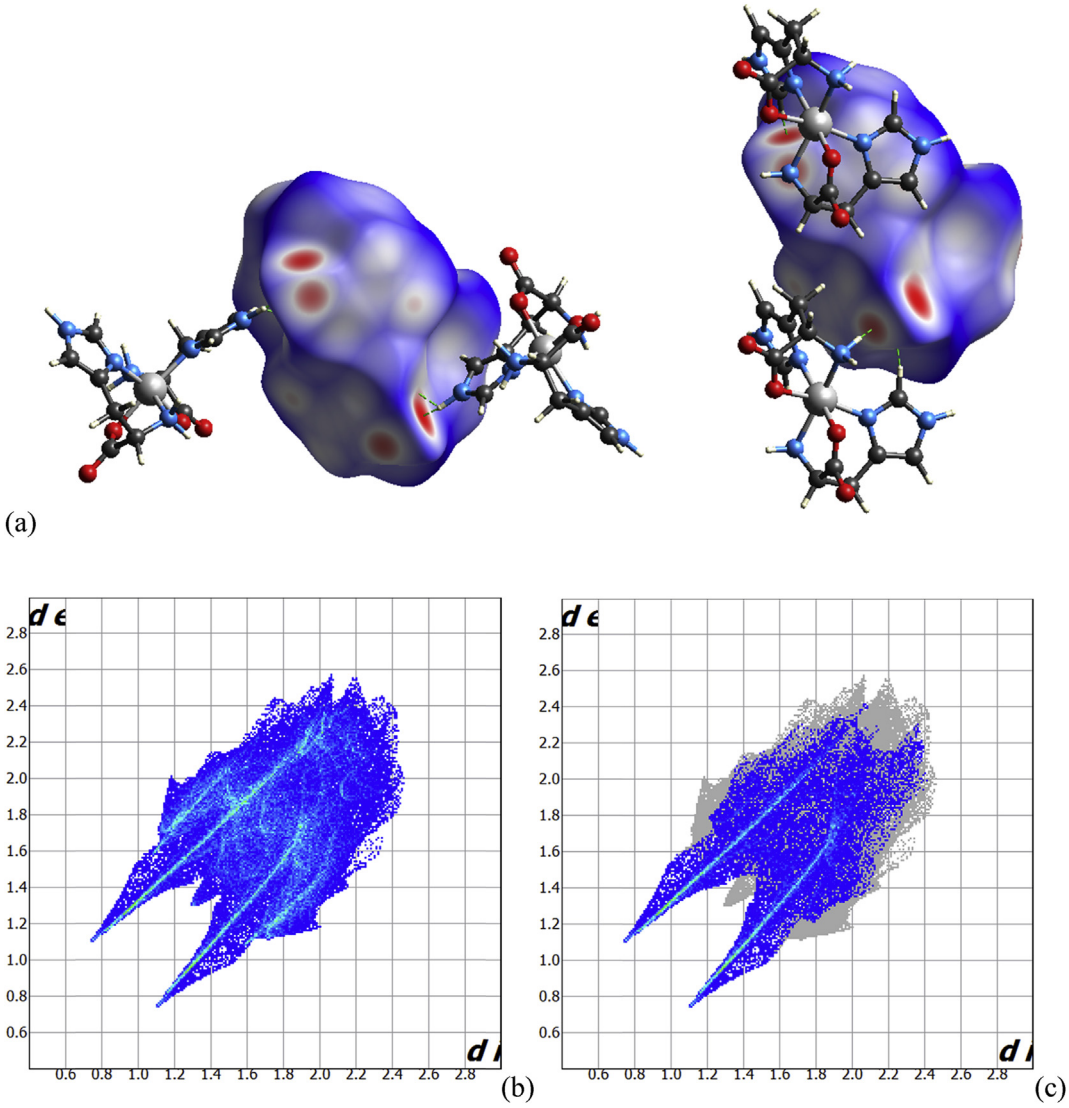

Fig. 5. Hirshfeld surfaces mapped with d_{norm} for **1**. (a) Fingerprint plots, (b) hole, and (c) O···H/H···O highlighted.

crystal. The O···H/H···O intermolecular interactions appear as distinct spikes in the 2D plot. The fingerprint plots can highlight atom pair close contacts and enable one to separate different interaction types, which overlap in the full fingerprint. The sum of O···H/H···O interactions comprises 36.5% of the Hirshfeld surfaces. Furthermore, Hirshfeld surfaces show no sign of the presence of the intramolecular N–H···O weak interactions in the solid phase, although it is present in the gas phase.

4.3. QTAIM and reduced density gradient

The QTAIM approach proposed by Bader is the most refined method for the analysis of the topology of the electron density, which is repeatedly used for revealing and enlightening the bonding situation between the atoms [28,29]. Here, we used this method to gain insight into binding characteristics and to confirm the presence of N–H···O weak interactions in the gas phase structure. The data are shown in Table 4. Although QTAIM shows no critical point for the intramolecular N–H···O weak interactions in the gas phase, the delocalization index for this bond in the gas phase shows some degree of electron sharing for a weak interaction between hydrogen and nitrogen. The delocalization index values in the gas phase are twice those in the solvent (Table 5), which confirms the presence of a weak interaction in the gas phase. Recently, it has been suggested that for weak intramolecular hydrogen bonds, the QTAIM analysis may show no bond critical points [30], and in these cases one might use the reduced density gradient analysis [31]. This analysis confirmed the presence of intramolecular N–H···O weak interactions in the gas phase. Gradient isosurfaces for the N–H···O weak interaction are shown in Fig. 6. The isosurface represents the weak interaction area clearly, although this interaction is categorized as weak. Repeating this analysis on the solvent-optimized structure revealed that such interaction is not present in solvent.

Table 4
Bond critical point electron densities (ρ), their Laplacian ($\nabla^2\rho$), and ellipticities (ε).

	ρ	$\nabla^2\rho$	ε
$Bond_{(pyridine\ solvent)}$			
Ni_2–O_8	0.063	0.309	0.015
Ni_2–N_{13}	0.070	0.294	0.072
Ni_2–N_5	0.066	0.303	0.037
O_8–C_{30}	0.362	−0.554	0.091
C_{30}–C_{16}	0.251	−0.647	0.096
C_{16}–N_{13}	0.255	−0.627	0.029
C_{16}–C_{41}	0.245	−0.610	0.025
C_{30}–O_1	0.392	−0.406	0.104
C_{41}–C_{20}	0.259	−0.687	0.058
C_{20}–N_5	0.311	−0.907	0.169
C_{20}–C_{40}	0.331	−0.965	0.359
C_{22}–N_5	0.360	−1.117	0.290
C_{22}–N_{21}	0.329	−0.885	0.263
C_{40}–N_{21}	0.305	−0.756	0.199
$Bond_{(gas\ phase)}$			
Ni_2–O_8	0.071	0.346	0.005
Ni_2–N_{13}	0.069	0.288	0.090
Ni_2–N_5	0.061	0.283	0.050
O_8–C_{30}	0.356	−0.577	0.101
C_{30}–C_{16}	0.244	−0.610	0.095
C_{16}–N_{13}	0.254	−0.623	0.030
C_{16}–C_{41}	0.246	−0.616	0.031
C_{30}–O_1	0.406	−0.311	0.130
C_{41}–C_{20}	0.259	−0.689	0.050
C_{20}–N_5	0.311	−0.912	0.158
C_{20}–C_{40}	0.331	−0.971	0.358
C_{22}–N_5	0.365	−1.200	0.302
C_{22}–N_{21}	0.323	−0.854	0.264
C_{40}–N_{21}	0.301	−0.725	0.209

Table 5
Calculated delocalization index for intermolecular hydrogen bonds.

Bond	$\delta(A\cdots B)_{Gas\ phase}$	$\delta(A\cdots B)_{Pyridine}$
N_{13a}–H···O_8	0.0217	0.0117
N_{13}–H···O_{8a}	0.0217	0.0117

4.4. Spectroscopic studies

Because of insolubility of the titled compound in common solvents, solid state ultraviolet–visible (UV–vis) spectrum was recorded in the 200–700 nm range, and the electronic absorption spectrum was calculated using the gas phase and pyridine optimized geometries with TD-DFT method. We used the B3P86 functional and the def2-TZVP basis sets with C_2 symmetry. The same calculations were carried out using the solid-state geometry without optimization (see Fig. 7).

The calculated electronic absorption spectra of **1** in the solid and gas phases and pyridine together with solid state UV–vis spectrum reveal that different distortions from octahedral geometry in the gas phase, pyridine, and the solid phase for **1** result in different electronic absorption spectrum in each phase. Calculation of electronic absorption spectra using solid-state geometry without optimization results in a spectrum, which is in good agreement with experimental data (Fig. 8). Repeating the same calculations with PBE0 functional gives similar result as B3P86.

Electronic absorption spectrum of **1** in solid state (Fig. 8) shows several bands roughly around 240, 290, 350, and 540 nm. By investigating the percentage weights of the molecular orbitals involved in electronic excitations, we found that in the band around 500–600 nm, there are contributions from three types of electronic excitations, that is, metal-to-ligand charge transfer, intraligand transitions, and metal d–d transitions. Furthermore, TD-DFT calculation results suggest that band around 500–580

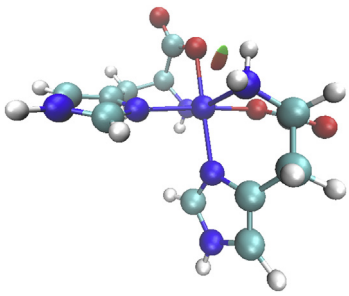

Fig. 6. Gradient isosurfaces ($s = 0.35$) showing weak intramolecular interaction present in the gas phase.

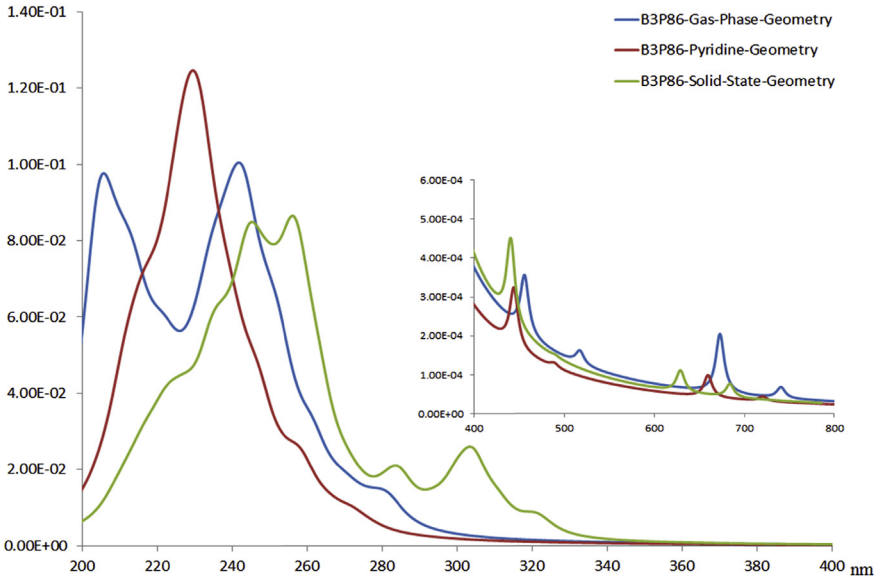

Fig. 7. Calculated electronic absorption spectra using the gas phase, pyridine, and solid-state geometries with TD-DFT method using B3P86 functional.

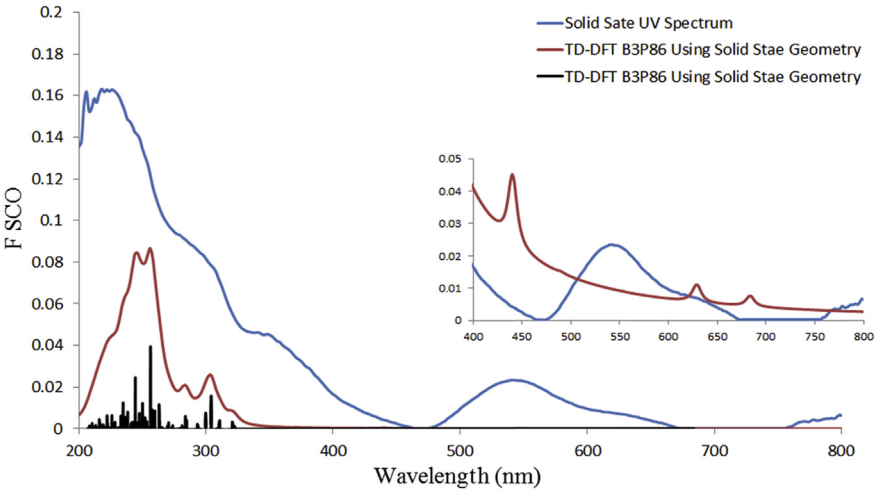

Fig. 8. Solid-state UV–vis spectrum and calculated spectrum using B386 applying def2-TZVP basis set 200–800 nm.

mainly related to the transitions from HOMO-3 and HOMO-4 to LUMO, the band around 350 mainly related to the transitions from HOMO-12 and HOMO-11 to LUMO+1, and the band around 240 and 290 mainly related to the transition from HOMO and HOMO-1 to LUMO+2. The free histidine ligand has no absorption band at wavelength longer than 245 nm [32], which is consistent with our TD-DFT calculations on free ligand.

4.5. Frontier molecular orbitals

The frontier molecular orbitals (HOMO and LUMO) can determine molecular reactivity and its photophysical properties. The isodensity plots for the HOMOs and LUMOs orbitals are shown in Fig. 9. It can be seen that HOMO is mainly localized on the metal atom and on the 2-amino-propanoic acid part of the histidine ligand, whereas the LUMO is most on the imidazole ring and to a lesser extent on the metal. Because the first electron transfer occurs from the HOMO to LUMO, it can be inferred that the first low energy electronic transition is combined ligand to ligand charge transfer (LLCT) from organic moiety and d–d metal electron transition. By using HOMO and LUMO energy values for the molecule, electronegativity and chemical hardness and softness were estimated using well-known relations [33–36] and are reported in Table 6 along with the dipole moment of **1**.

5. Conclusions

A new bis(histidinato)nickel(II) has been synthesized, using solvothermal crystal growth. The resulting complex

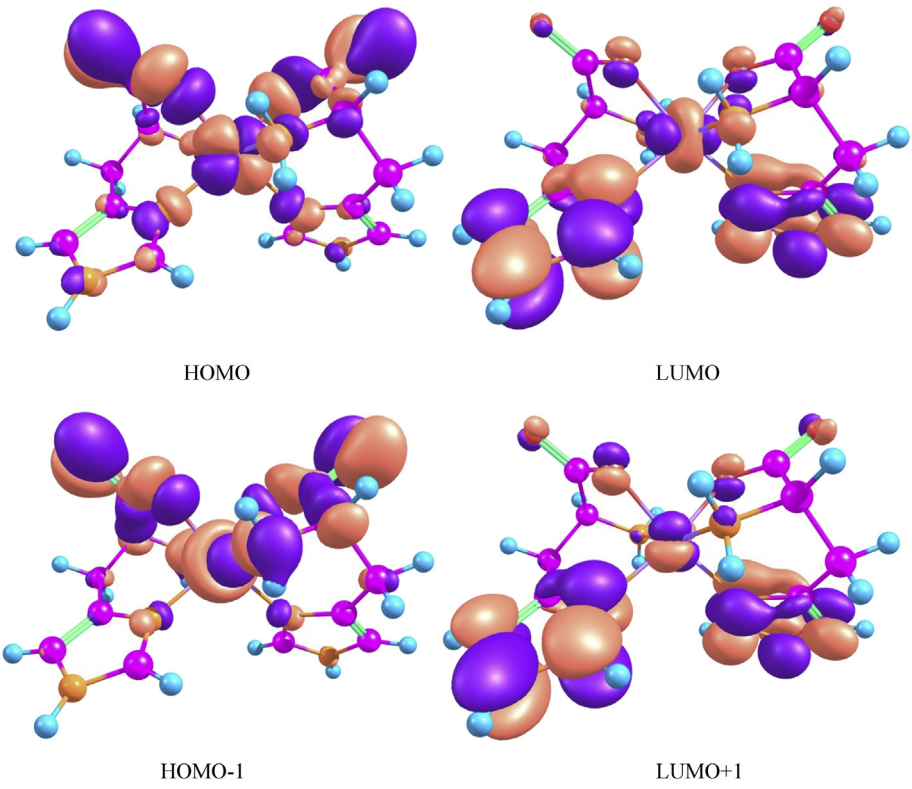

Fig. 9. The isodensity plots for HOMOs and LUMOs.

Table 6
Orbital energies, chemical hardness, chemical softness, electronegativity, and dipole moment of **1**.

PBE0/def2-TZVP	Gas phase ($\varepsilon = 1$)	Pyridine ($\varepsilon = 12.5$)	Water ($\varepsilon = 80.40$)
E_{HOMO} (eV)	−4.85	−5.26	−5.30
E_{LUMO} (eV)	−0.70	−0.22	−0.15
$\Delta E_{HOMO-LUMO}$	4.14	5.04	5.14
Chemical hardness (η)	2.07	2.52	2.57
Chemical softness (S)	0.24	0.20	0.19
Electronegativity (χ)	2.78	2.74	2.73
Dipole moment (Debye)	16.0	23.3	24.6

has distorted octahedral geometry. The title compound shows different octahedral distortions in the gas, liquid, and solid phases using geometry optimization in the gas phase and pyridine together with Hirshfeld surface and reduced density gradient analyses. This can be related to the presence of two weak intramolecular N–H···O weak interactions in the gas phase and two sets of rather strong intermolecular N–H···O and C–H···O interactions in the solid phase. Although intramolecular N–H···O weak interactions in the gas phase are not confirmed by QTAIM analysis, the reduced density gradient and delocalization indices approve this weak interaction. Furthermore, TD-DFT calculations suggest that these different distortions result in different electronic absorption spectrum in each phase.

Acknowledgments

The authors appreciate the University of Tehran for financial support.

References

[1] A.K. Sengupta, O.P. Bajaj, U. Chandra, J. Indian Chem. Soc. 55 (1978) 962.
[2] H. Singh, L.D.S. Yadav, B.K.J. Battacharya, J. Indian Chem. Soc. 56 (1979) 1013.
[3] S. Giri, H. Singh, L.D.S. Yadav, R.K. Khare, J. Indian Chem. Soc. 55 (1978) 168.
[4] A. Cansiz, S. Servi, M. Koparir, M. Altintas, M. Digrak, J. Chem. Soc. 23 (2001) 237.
[5] I. Kostova, Curr. Med. Chem. 13 (2006) 1085–1107.
[6] T. Ishiyama, J. Takagi, J.F. Hartwig, N. Miyaura, Angew. Chem., Int. Ed. 41 (2002) 3056.
[7] J. Breitenfeld, R. Scopelliti, X. Hu, Organometallics 31 (2012) 2128.
[8] A.M.A. Alaghaz, M.E. Zayed, S.A. Alharbi, R.A. Ammar, A. Elhenawy, J. Mol. Struct. 1084 (2015) 352.
[9] J.D. Kopple, M.E. Swendseid, J. Clin. Invest. 55 (1975) 881.
[10] F.A. Carey, Organic Chemistry, 4th ed., McGraw-Hill, 2000, p. 868.
[11] M. Agnieszka, K.W. Janina, K. Katarzyna, J. Mol. Struct. 655 (2003) 397.
[12] L. Wang, Na. Sun, T. Simon, Z. Xuejun, D.R. Benson, Biochemistry 45 (2006) 13750.
[13] R.H. Blessing, E.L. McGandy, J. Am. Chem. Soc. 94 (1972) 4034.
[14] R.A. Laudise, R.L. Barns, IEEE Trans. Ultrason. Ferr. 35 (1988) 277.
[15] F. Senn, L. Helm, A. Borel, C.A. Daul, C. R. Chim. 15 (2012) 250.

[16] A. Elkechai, A. Boucekkine, L. Belkhiri, D. Hauchard, C. Clappe, M. Ephritikhine, C. R. Chim. 13 (2010) 860.
[17] D. Farmanzadeh, T. Abdollahi, M. Jafary, C. R. Chim. 19 (2016) 579.
[18] G.M. Sheldrick, Acta Crystallogr., A 64 (2008) 112.
[19] F. Neese, Comput. Mol. Sci. 2 (2012) 73.
[20] T. Lu, F. Chen, J. Comput. Chem. 33 (2012) 580.
[21] M.A. Spackman, D. Jayatilaka, Cryst. Eng. Commun. 11 (2009) 19.
[22] F.L. Hirshfeld, Theor. Chim. Acta 44 (1977) 129.
[23] H.F. Clausen, M.S. Chevallier, M.A. Spackman, B.B. Iversen, New J. Chem. 34 (2010) 193.
[24] A.L. Rohl, M. Moret, W. Kaminsky, K. Claborn, J.J. McKinnon, B. Kahr, Cryst. Growth Des. 8 (2008) 4517.
[25] A. Parkin, G. Barr, W. Dong, C.J. Gilmore, D. Jayatilaka, J.J. McKinnon, M.A. Spackman, C.C. Wilson, Cryst. Eng. Commun. 9 (2007) 648.
[26] M.A. Spackman, J.J. McKinnon, Cryst. Eng. Commun. 4 (2002) 378.
[27] S.K. Wolff, D.J. Grimwood, J.J. McKinnon, D. Jayatilaka, M.A. Spackman, CrystalExplorer 2.0, University of Western Australia, Perth, Australia, 2007.
[28] R.F.W. Bader, Atoms in Molecules a Quantum Theory, Oxford University Press, Oxford, UK, 1990.
[29] C.F. Matta, R.J. Boyd, The Quantum Theory of Atoms in Molecules. From Solid State to DNA and Drug Design, Wiley-VCH, 2007.
[30] J.R. Lane, J. Contreras-García, J.P. Piquemal, B.J. Miller, H.G. Kjaergaard, J. Chem. Theory Comput. 9 (2013) 3263.
[31] E.R. Johnson, S. Keinan, P. Mori-Sánchez, J. Contreras-García, A.J. Cohen, W. Yang, J. Am. Chem. Soc. 9 (2010) 6498.
[32] J.M. Dixon, M. Taniguchi, J.S. Lindsey, Photochem. Photobiol. 81 (2005) 212–221.
[33] Z. Demircioglu, Ç. Albayrak, O. Büyükgüngör, J. Mol. Struct. 1065–1066 (2014) 210.
[34] N. Özdemir, S. Dayan, O. Dayan, M. Dinçer, N.Ö. Kalaycıoglu, Mol. Phys. 111 (2013) 707.
[35] H. Tanak, A.A. Agar, O. Büyükgüngör, J. Mol. Struct. 1048 (2013) 41.
[36] H. Pir, N. Günay, D. Avcı, Y. Atalay, Spectrochim. Acta, Part A 96 (2012) 916.